Materials and methods

Gold support fabrication

The foils are fabricated by thermal evaporation of pure gold on a holey carbon template layer, with subsequent removal of the carbon using an argon-oxygen plasma. To create the gold substrate, we started with a Quantifoil Au 300 1.2/1.3 support, placed it carbon side up in a vacuum evaporator (Edwards 308 turbo), equipped with a turbo pump, a liquid nitrogen cold trap and an in-situ crystal thickness monitor (Inficon), evacuated it to a base pressure of 1×10^{-7} torr, and then deposited the specified thickness layer of gold (EMS, 99.99%) by thermal evaporation at $\sim$1 Å/s. The residual pressure in the chamber during evaporation of the gold was $\sim1\times10^{-5}$ torr. During evaporation, the grids were supported on a glass slide, whose concurrent gold coating was then used for subsequent AFM thickness measurements. We tested a range of thicknesses and found 400-500 Å was optimal as it minimized motion as much as thicker layers (fig. S10) but still gave thin ice films under typical blotting conditions. Below 400 Å, the performance of the gold support foils began to degrade. We believe that once the thickness of the film becomes comparable to the average diameter of the grains in the polycrystalline metal, the film no longer maintains a uniform contact between grains and the mechanical and electrical properties are degraded. Thinner films with good performance are likely possible if a smaller polycrystalline grain structure or a single crystal is maintained during the growth of the metal film.

After evaporation of gold, the grids were removed from the chamber and loaded into a custom suspension holder in a low-energy plasma chamber (Fischione 1070) and evacuated to $\ll10^{-4}$ torr. High purity argon and oxygen (BOC 99.9999%) were admitted in a ratio 9:1 to a pressure of 21 mtorr, and a radio frequency plasma was generated with 38 W of forward power and $\leq$ 2 W of reverse power, which was applied to the grids for 30 minutes. This was sufficient to remove all exposed carbon from the support layer. The grids were then stored in a low-humidity, dust-free container until used. We calibrated the amorphous carbon etch rate for these plasma conditions by etching thin films of carbon and measuring the change in thickness vs. dose and found that under these conditions it was 3 Å/s. No gold etching by the plasma was detectable even after long doses. Note that this process leaves some residual carbon between the gold layer and the grid bar. We also made grids where the gold layer was added to the other side of the template layer, thus eliminating all carbon after plasma treatment, but there was no difference in the performance of the grids made in this way vs. the carbon-side up, and the process of carbon-side down fabrication was less reliable and more difficult. So we instead use the carbon-side up approach described above. Using this method with standard commercial equipment, we can produce $\sim$50 grids in less than a day.

Atomic force microscopy

The thicknesses of gold films were measured using an atomic force microscope (Asylum MFP3D) operated in constant force mode where the tip is maintained in contact with the sample as it is scanned in-plane. First, the gold film which was deposited on a glass slide during evaporation was cleaved using adhesive tape (3M Scotch Crystal) and the resulting step edge was imaged. For a

typical scan, an oxide-sharpened silicon tip on a silicon cantilever with a force constant of $\simeq$0.3−0.8 N/m (Mikromasch CSC37) was used to scan the area covering the edge. The scan rate was 0.3 (fig. S1 and fig. S10) or 0.1 Hz (fig. S9) and the images were (1024 or 512 px)^2, over an area of (10 or 20 μm)^2 respectively. The images were masked and flattened using second order polynomials, fit to the support glass. A histogram of the heights was then used to measure the thickness and roughness in the following way: The peak for the substrate surface and the foil surface were fit with Gaussian functions, and the composite error in locating the position of the two peaks was taken as the error in the average thickness of the foil. The width (standard deviation) of the fit to the peak on the gold surface was then taken as an approximation of the surface roughness.

Force measurements (fig. S9) were conducted using the same microscope, but with a softer silicon nitride cantilever, whose force constant was nominally 0.02 N/m (Asylum BL-TR400PB) and was calibrated using thermal oscillation (*28*) where the absolute error is ∼5%. First the grid square of interest was inspected optically and the center was located using a low-magnification overview scan. Then the tip was placed on the center and F vs z curves collected using a maximum force setpoint. After collection, the region was re-imaged to verify that no damage to the foil occurred. Each extension force curve, where the tip was pushed into the surface, was fit to a line in the region where the tip was in hard contact with the surface, from 0 to 2 nN. The slopes for the multiple measurements were then averaged and the standard deviation was taken as the error.

Grid motion tracking

The vertical motion of the perforated foil was determined using am-C (Quantifoil Au 300 R1.2/1.3) or gold supports of the same geometry. For the data in Fig 2A, the grids were used as manufactured. For the data in Fig. 2B, supports were treated with a 9:1 argon:oxygen plasma for 18−20 seconds and immediately placed in a cryo-plunger (FEI Vitrobot III) equilibrated to 4 °C and 100% relative humidity. We have also used glow discharge to render gold grids sufficiently hydrophilic for the application of aqueous solutions. In general we found that appropriate plasma and glow discharge conditions were the same for gold and am-C supports. 3 μl of aqueous protein solution was applied, allowed to incubate for 15 s, blotted with force setting −2 mm for 4−6 s, and then plunged into liquid ethane at just above its melting point. Grids were stored in liquid nitrogen until they were used. All samples were then transferred to an FEI Titan Krios microscope, and maintained at 80−90K. The goniometer was tilted to 30 ° and images were obtained by illuminating an individual 1.2 μm diameter hole, where the beam was centered on the hole and included a region of the support around the perimeter as described previously (*17*). The beam diameter was 1.7 μm and we used 300 keV electrons, a nominal magnification of 27k × and 16 e$^-$/Å^2/s. Images were recorded for 4 s using a direct-electron detector (FEI Falcon II) with a frame rate of 18 frames per second. Because of incomplete blanking of the beam, the first and last frames of the movie are discarded. The edge of the hole on the axis perpendicular to the tilt axis was tracked in ImageJ (*29*) by integrating the intensities over a 100 pixel wide section and manually selecting the edge location in each frame. The amount of membrane displacement in the image was converted to membrane displacement in the z direction (the direction perpendicular to the plane of the support). For the data in Fig. 2A, 18,

17 or 29 hole edges were tracked, each from 3 different grid squares on one of three different am-C grids. On the three different gold grids, 32, 18 or 18 hole edges were tracked in 4, 3 or 3 grid squares respectively. For the data in Fig. 2B, three different am-C grids were examined and 10, 21 or 18 hole edges were tracked in 1, 3 or 3 different grid squares respectively. Three different gold grids were examined and 18, 16 or 9 hole edges were tracked in 3, 3 or 1 grid squares respectively.

Ribosome tracking and determination of κ

To determine the in-plane (x/y motion) of proteins suspended in ice, movie collection and tracking of ribosomes was performed as described in (*17*) using *Saccharomyces cerevisiae* 80S ribosomes provided by the V. Ramakrishnan lab. Images were taken using an FEI Titan Krios at 300 keV with standard cryo-EM low-dose conditions (16 $e^-/Å^2/s$, less than 0.2 $e^-/Å^2$ preexposure in low-mag mode, 80−90 K) and using a back-thinned direct-electron detector (Falcon II) as above. Importantly, images were obtained by illuminating an individual 1.2 μm diameter hole, where the beam was centered on the hole and included a circularly symmetric ring of the support around the perimeter of $\simeq$250 nm (*17*). Furthermore, for all experiments, any grid squares with cracks or other defects were not used. 1236 particles from 101 holes on 3 gold grids were analyzed. The only difference from the previously published data collection methods was the determination of focus during low-dose imaging. Since there is no amorphous material in the gold support structure, phase contrast rings in the real-time diffractogram cannot be used to find the Gaussian focus point. Instead, at least four other options are available: 1. The beam can be brought into convergence and the distance between the diffracted beams in the imaging plane is minimized when the grid is in focus. 2. The ronchigram from the convergent beam diffraction pattern can be used to set the focus. 3. Using a parallel illumination beam, diffracted beams from individual gold crystals induce a positive contrast region, whose distance from the particular crystal of origin increases with the magnitude of defocus. So the plane of focus is found by bringing this region into convergence with the matching crystal of origin. 4. In bright field imaging mode, the beam tilt can be wobbled about its minimum value; when the resultant image shift amplitude is at a minimum, the sample is in focus. In practice, focusing using any of these methods is at least as fast and easy as focusing using fast Fourier transforms of images of amorphous material, particularly due to the high contrast of the gold and the fact that no real time Fourier transforms are needed, and each can be done on a phosphor screen instead of a camera. We note that beam tilt and first order stigmation were generally aligned using a standard test specimen, and then only fine-tuned during data collection. Particles on am-C supports (Fig. 3A and fig. S2) are from Russo and Passmore (*17*).

Tilt-pairs were collected using a tilt of 30 °. The pixel size was (1.34 or 1.78 Å)^2 at the sample. Particles were picked using either manual picking or a semi-automated swarm procedure in EMAN2, and preprocessed in Relion (*24*). Micrograph contrast transfer function parameters were determined by fitting using CTFFIND (*30*), and parameters from the measurements in (*13*) were used to correct for the modulation transfer function of the detector. 2D classification and 3D refinement were carried out in Relion with an initial model low-pass filtered to 50 Å. To measure the motion of the ribosomes in speed plots, five-frame running averages were used to determine the ribosome positions for each

frame, then the RMS particle displacements were calculated for an entire ensemble of ribosomes from a single grid (dotted line, fig. S2) versus time/dose. The mean trajectories for each support were calculated and are plotted as a solid line (fig. S2). The Euler angles assigned to each particle in Relion at each iteration of map refinement were extracted and the angular difference between each pair of particle images was calculated with tiltdiffmulti/tiltStats (*5, 20, 31*). The concentration parameter κ and the angular accuracy were determined using tiltStats (*20*) and plotted vs. iteration (fig. S5). Per-frame B factors for fig. S3 were calculated with Relion (*32*) using five-frame running averages with a dataset which included particles from the previously published dataset imaged on graphene (*17*) to improve the orientation distribution and coverage of Fourier space.

Cryo-EM of apoferritin

Grid preparation

Horse (*Equus caballus*) spleen apoferritin was obtained from Sigma and diluted to 8 μM (3.5 mg/ml) in phosphate-buffered saline, pH 7.4. Vitrified samples were prepared as above, using the same conditions for gold and am-C.

Imaging and data collection

Vitrified apoferritin was imaged with 300 keV electrons in a FEI Polara under low-dose conditions (16 $e^-/Å^2/s$, less than 0.2 $e^-/Å^2$ preexposure in low-mag mode, 80−90 K) at a nominal magnification of 59k × (104k × actual) using the illumination geometry described above. Exposures were 1 s on a direct electron detector (FEI back-thinned Falcon II) for which the frame rate was 17 frames per second, and calibrated pixels corresponded to $(1.346\ Å)^2$. Micrographs were gain-corrected after collection by division by the sum of all the images, normalized to the mean value. Tilt-pairs were collected using a tilt of 30 °.

Single particle data analysis and modeling

Particles were picked from micrographs using EMAN2, then preprocessed and extracted into boxes of 132 × 132 pixels using Relion and CTFFIND. Two-dimensional classification was used to remove particles that didn't align well with each other, and the remaining particles were used for 3D refinement in Relion. A density map was calculated from a crystal structure of apoferritin (PDB 1IER (*33*)) using EMAN, and was low-pass filtered to 40 Å and used as the initial model for 3D refinement using Relion. Three different datasets were analyzed. Apoferritin was imaged on both am-C and gold supports, on the same day, on the same microscope (Polara equipped with a Falcon II at the MPI Frankfurt) with samples prepared identically at the same time on both gold and am-C grids. After 2D classification where 6% of the picked particles were removed from each dataset, there were 3995 apoferritin particles on am-C and 3756 particles on gold supports. Each set was processed identically in Relion and the reconstructed maps calculated using 3D refinement where the data were split into two random halves, and each half is kept separate throughout the reconstruction process (*24*). The

reconstructed maps had resolutions of ∼25 Å and ∼8 Å respectively (Fig. 3B-C). We also tried motion correction algorithms on the whole micrograph (*2, 16*) and on individual particles (*15, 34*) but were unable to improve the images enough to align the particles.

A third, larger dataset was collected using a Polara with a Falcon II at LMB on gold which had 5968 particles after automated picking and 2D classification. The reconstructed 3D map from these particles had a resolution of ∼7 Å (fig. S6). We performed two rounds of 3D classification (*24*) on the particles from this third dataset. The first had three classes and after 20 iterations, one class was selected containing 2903 particles. These were further classified in a second round that had four classes. After 11 iterations, the best class (with 483 particles), shown in the fig. S6, had better density around the dimer interface and was chosen for refinement. The resolution was not restricted during the 2 rounds of 3D classification. These particles were then used to calculate a 3D reconstruction in Relion using 3Dautorefine (after splitting the data into two random halves and keeping each separate throughout the reconstruction process) using the 3D map from the larger dataset, low-pass filtered to 25 Å. After refinement, individual movie frames for each particle were used to calculate reconstructions for each frame, and then calculate B factors for each frame of data collection. A smooth polynomial fit to these relative B factors was then used to weight each frame and a calculate a final density map using Relion (*32*). No motion correction was applied at any stage of the apoferritin data analysis or refinement since this did not improve the maps. The final map had an overall resolution of 4.6 (0.143 FSC, as calculated with Relion postprocess using automated masking) or 4.7 Å (vs. crystal structure at 0.5 FSC calculated using Xmipp (*35*)) (fig. S7) and had an overall B factor of 165 Å^2 as calculated from fits to the Guinier plots after MTF correction (*5*).

Apoferritin tilt pairs were incorporated into a refinement, the Euler angles assigned to each particle were extracted and the angular difference between each pair of particle images was calculated with Tiltdiffmulti (*5, 20, 31*). There were 823 tilt pairs; 403 had angles greater than 6 ° out of plane and were therefore discarded. Here, ∼3.6% of the tilt pairs cluster around 30 ° which is in agreement with the proportion of particles (8%) used to obtain the final 3D reconstruction. We note that for tilt pairs both images of the pair need to be correctly aligned for the calculated tilt angle to match the true tilt angle.

The masked and unmasked maps and half maps are deposited in the EM DataBank with accession code 2788. The local resolution of the map in real space was calculated with ResMap at a confidence interval of $p = 0.05$ (*36*). We fit the high resolution crystal structure of apoferritin (2W0O, (*25*)) in the EM density map using rigid body fitting with MolRep (*37*). We also refined the previous model using the new cryo-EM density map with RefMac (*38*) using the resolution range 177−4.5 Å (Table S1), and the coordinates are deposited in the PDB with accession code 4v1w. Illustrations of 3D maps and models were rendered using UCSF Chimera (*39*).

Supplementary figures

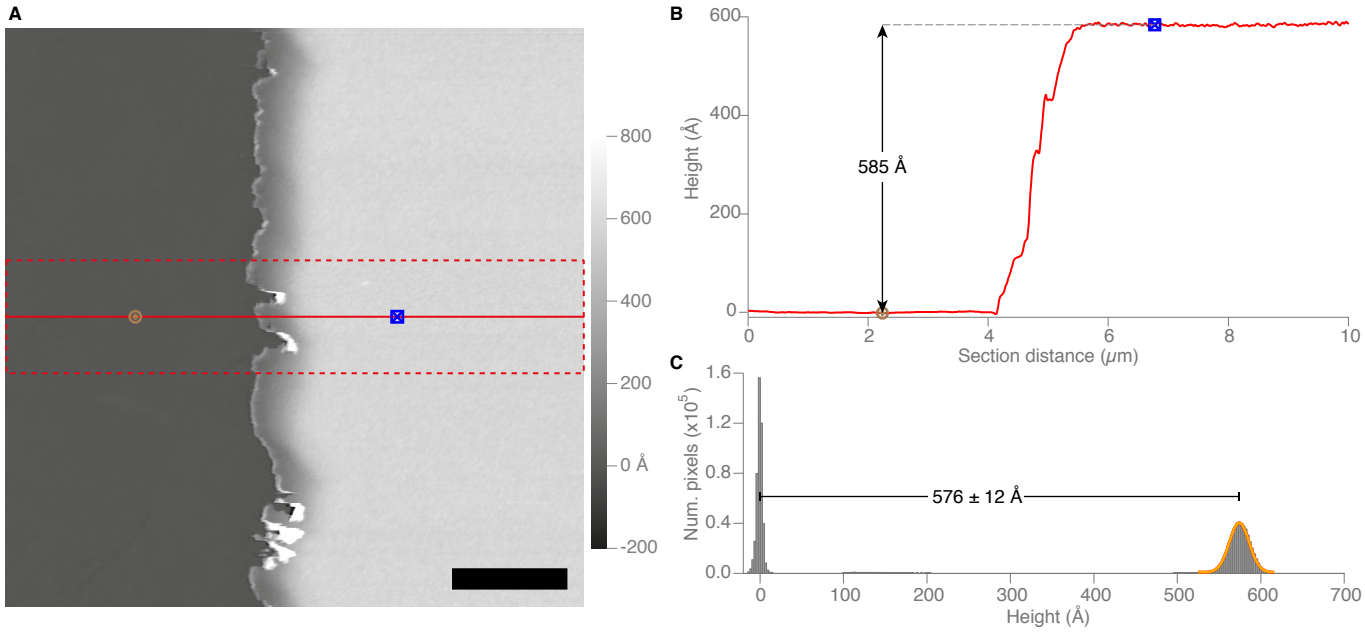

Fig. S1: **AFM thickness measurement of gold foil.** (**A**) Constant-force mode atomic force microscopy (AFM) topography image of gold as evaporated onto a glass slide during preparation of the perforated gold foil used for apoferritin. The continuous layer was cleaved off the support glass, and then the cleaved edge was imaged. Scale bar is 2 μm. Panel (**B**) shows the 100 pixel wide section indicated in (**A**) with vertical distance between the two points indicated. Panel (**C**) contains a histogram of the height values in (**A**), with Gaussian fits to determine the average thickness of the gold layer (576.2 $\pm$ 0.1Å). The standard deviation of the gold height is taken as the approximate roughness of the foil ($\pm$ 12 Å). The absolute error in the calibration of the z channel of the microscope is $\leq$ 1% or about 6 Å.

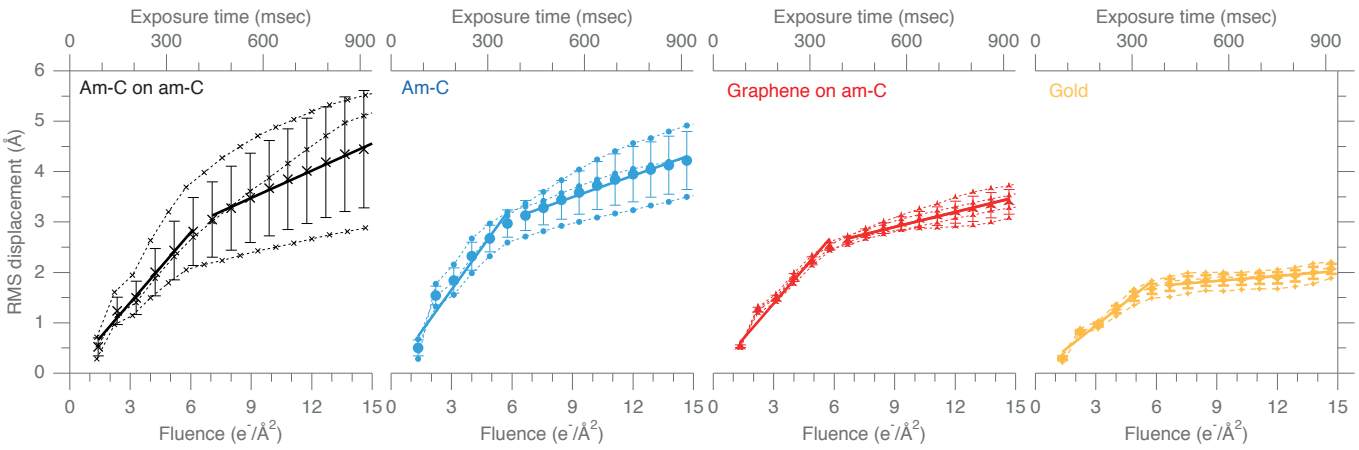

Fig. S2: **Speed plots of ribosomes on various substrates.** Root mean squared (RMS) ribosome displacement in ice from the initial position during electron beam irradiation is measured for different substrates: perforated am-C foil with an additional layer of am-C (black), perforated am-C foil (blue), perforated am-C foil covered with hydrogen plasma-treated graphene (red) and perforated gold foil (gold). 80S ribosome positions were measured using a five-frame running average under constant electron beam irradiation (300 keV; 16 $e^-/Å^2/s$). Data from the first three panels are from Russo and Passmore (*17*). Each point (dotted lines) is the RMS displacement of thousands of ribosomes from a single grid. Solid lines are linear fits. Error bars are the standard error of the mean of the replicate experiments. The ribosomes exhibit two phases of motion: an initial faster phase followed by a second slower phase. Relative to am-C, the first phase of motion on gold is reduced by 43% and the second phase is reduced by 77%.

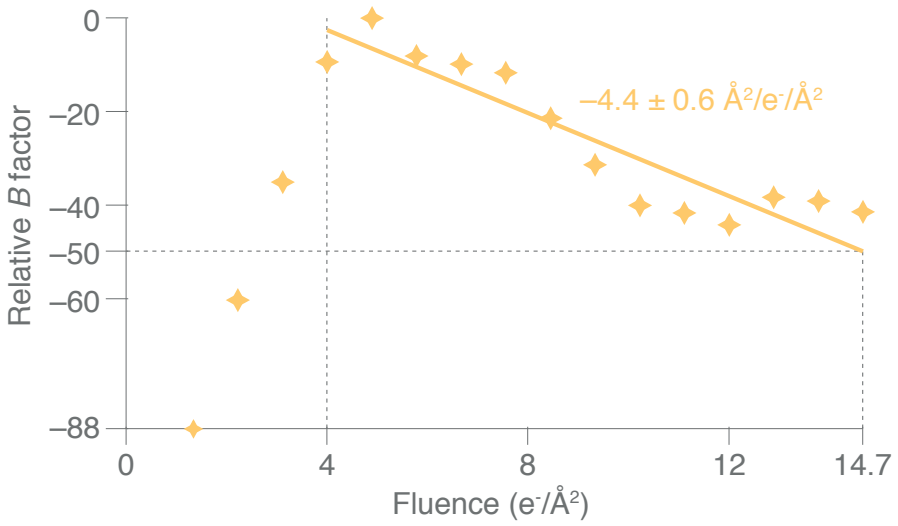

Fig. S3: ***B* factor vs. fluence.** B factors are empirically-determined parameters that provide a measure of image quality. The decay in B factor with dose should reflect changes in the sample. This includes radiation damage to the structures of the molecules themselves, to the movement of the particles during irradiation and any non-constant buildup of charge on the specimens that may affect the contrast in the images. This is based on the reasonable assumption that all the other sources of contrast loss, like detector efficiency and the imaging transfer functions of the optics remain constant during image acquisition. Perfect, non-charging, stationary specimens would then only exhibit a fluence dependent loss of contrast due to radiation damage to the molecules. If we take the fading of diffraction spots of 2D protein crystals (*27*) as an estimate of the radiation damage to stationary biological specimens, B factors decay with dose by approximately 4 $Å^2/e^-/Å^2$. Relative B factors for 80S ribosomes on gold supports (with some particles on graphene (*17*) added to improve the angular distribution of the dataset) were calculated using 5-frame running averages in Relion (*32*) and plotted against fluence. After exposure to the first 4 $e^-/Å^2$, ribosome B factors decay by 4.4 ± 0.6 $Å^2/e^-/Å^2$ and therefore approach those expected for radiation damage alone. This observation is congruous with the speed plots for gold substrates which show that after 4 $e^-/Å^2$, the particles are nearly stationary.

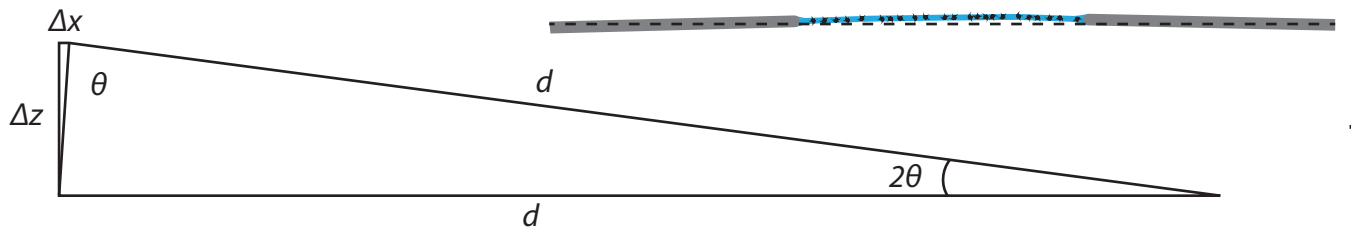

Fig. S4: **Model of coupling between motions in z and x/y.** We have measured the motion of am-C supports in the vertical (z) and horizontal (x/y) planes, and can thus compare these motions to those for gold, where the motion in z is negligible. For a thin foil where the thickness is much less than the width and length, it is reasonable to assume the that the force required bend the material away from its equilibrium position is much less than the force required to stretch the material in plane (*40*). Based on this assumption, and the difference in Δx_{amC} for particles on am-C, where the support moves vertically, vs. the in-plane motion on gold, Δx_{Au}, where it does not move vertically, one can make an order of magnitude estimate of the distance over which the ice-covered carbon bends, d, according to $d \sim (\Delta z_{amC} - \Delta z_{Au})^2 / [2(\Delta x_{amC} - \Delta x_{Au})]$. For the average displacement values in Figs. 2 & 3 the result is $d \sim 1200$ Å. This agrees with the length scale over which the substrate is irradiated, suggesting that the force induced by the beam bends the material, thus displacing the particles from their original positions. We speculate that the electron beam causes this force through the complicated buildup of charge on and in the ice and am-C, both of which are insulators at 80K. In the case of the gold support, this movement is reduced for at least two reasons: 1. gold is an excellent conductor at 80K, thus eliminating the charge buildup in the support foil and thereby reducing the magnitude of the force on the substrate, 2. the lack of differential thermal contraction between the perforated foil and the support grid means that the foil's flexural rigidity is maintained after cryoplunging. The remaining motion of the particles on the gold supports is then likely due to the motion of the ice within the holes, and possibly the motion of the particles within the ice; we expect the latter is much less than the former. Reducing the in-plane motion of the ice within the holes another factor of 2-3 should bring the total particle motion to within the error of our ability to determine the location of the particles, thus eliminating the loss of structural information due to radiation-induced motion.

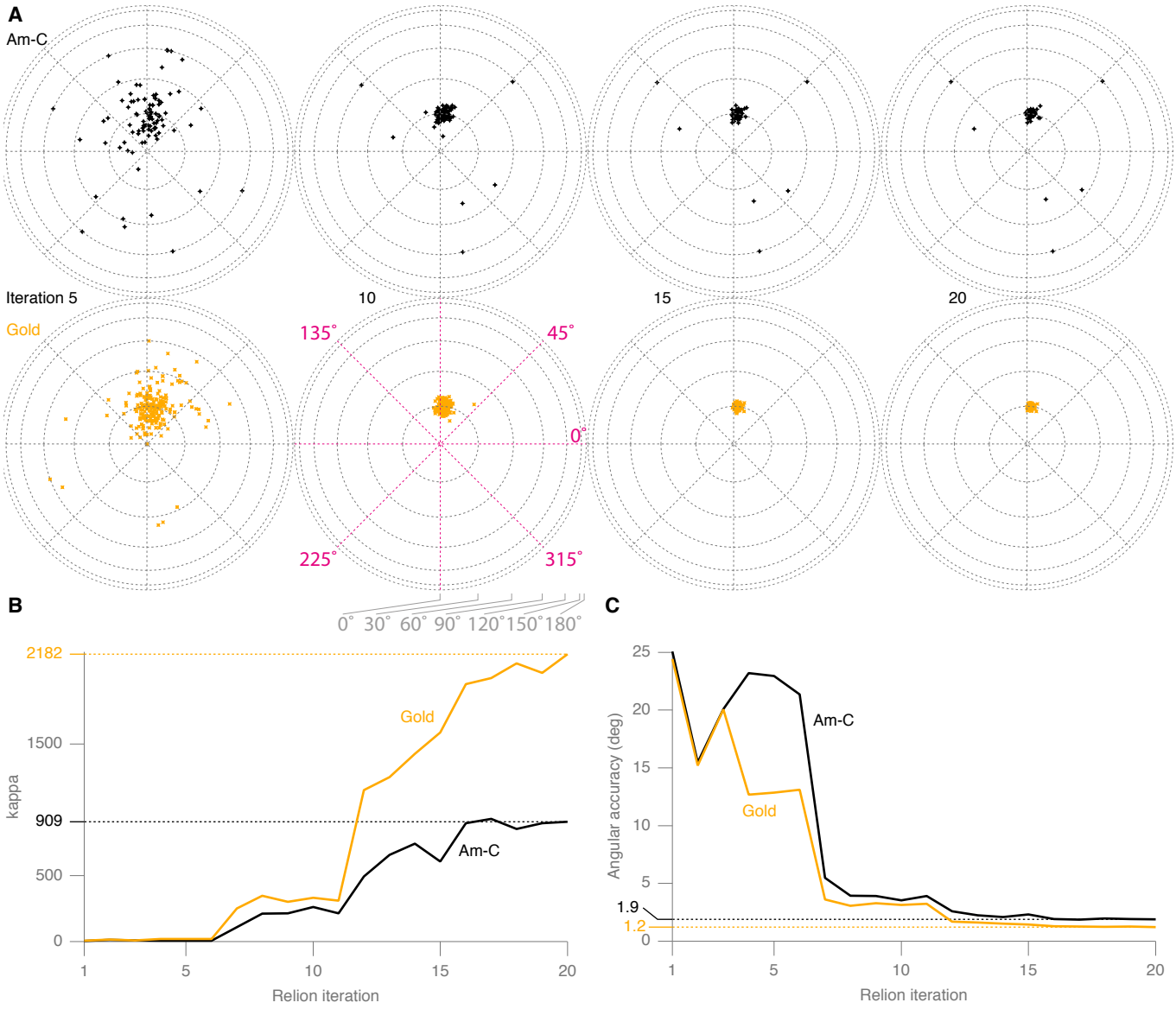

Fig. S5: κ **and angular accuracy for ribosomes on am-C vs. gold supports.** Pairs of images were collected for ribosomes on am-C (black) and gold (gold) supports under identical imaging conditions where the sample was at 0° and 30° tilt. The angles for all ribosome pairs were determined during map refinement using Relion, and the difference in the angles for image pairs was calculated with Tiltdiffmulti (*31*). These angles comprise a distribution of directions on the unit sphere which we plot using Lambert's equal area projection (**A**). The radius is the angle from 0° at the centre to 180° at the edge, and the azimuth is the direction of tilt. From these data, we calculate the concentration of the distribution (κ) at each iteration of refinement using tiltStats (**B**). κ is a direct measure of the quality of the images (*20*) and the use of gold supports leads to a higher κ. The accuracy of the angles assigned to the individual images during 3D reconstruction is improved and converges faster on gold compared to am-C supports (**C**).

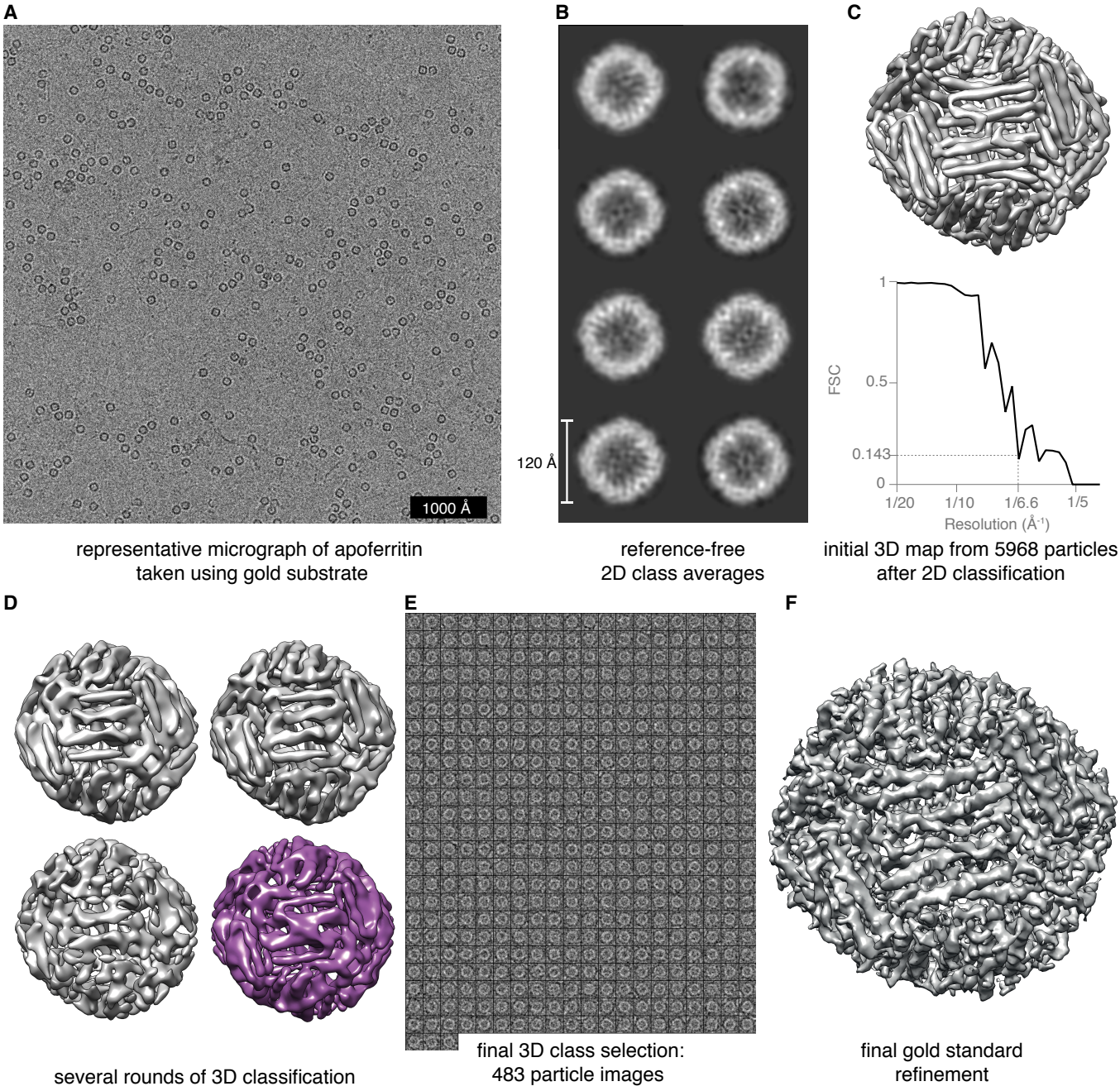

Fig. S6: **Image processing strategy for apoferritin.** (**A**) Apoferrtin suspended in ice on a gold support was imaged in an electron microscope equipped with a direct electron detector (Falcon II) under typical cryo-EM illumination conditions (300 keV, 16 $e^-/Å^2/s$, 1s exposures and 80K). The original image with 16 bits of native resolution was cropped to 3600 × 3600 pixels (1.78 Å/px) and intensity was scaled to an 8-bit window comprising ± 3σ about the mean intensity value. (**B**) Reference-free 2D class averages of individual particle images reveal α-helices. Particles in classes lacking these high-resolution features were discarded in an iterative procedure. (**C**) An initial 3D reconstruction from 5968 particles had a resolution of 6.6 Å. (**D**) Two rounds of 3D classification in Relion separated out several conformations of apoferritin with differences in the density associated with a surface loop. The classes from the last round of classification are shown. (**E**) The 483 particles from the purple class in (**D**) were selected and a 3D reconstruction with resolution 4.6 Å was obtained (**F**) .

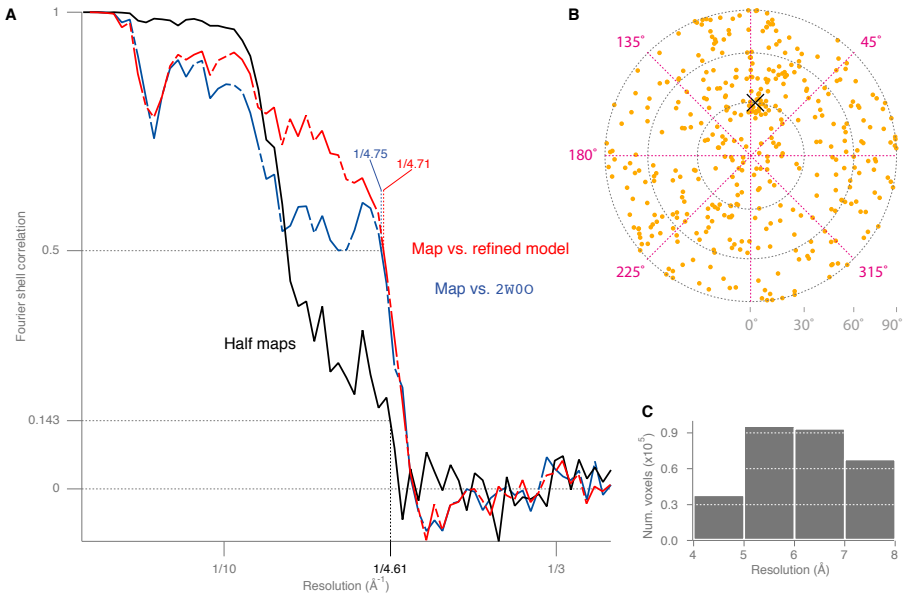

Fig. S7: **Validation and resolution of the apoferritin map.** (**A**) Fourier shell correlation coefficients were calculated between two random halves of the data (black solid line), where each half is kept separate throughout the reconstruction process (*24*). The Fourier shell correlation was also calculated between the EM map and a previously published crystal structure of apoferritin (PDB 2W0O) (*25*) (blue single dashed line), and between the EM map and the refined model reported here (red double dashed line). The refinement was limited to 4.5 Å; the refined model shows an improved correlation with the map, which is likely at least partially indicative of a different conformational state of the complex relative to the previous structure. Although there is currently no mathematically rigorous way to determine the degree of overfitting when refining against EM density maps, inspection of the refined model within the map shows a clear improvement in the fits of individual side-chains into the density protrusions along the helices, and the overall contour of the molecular chain is a better match to the density contour. The overall resolution of the map is 4.7 Å. (**B**) Pairs of images were collected where the sample was at 0° and 30° tilt. The angles for all apoferritin pairs without any classification or selection were determined using Relion, and the difference in the angles for image pairs was calculated with Tiltdiffmulti (*31*). These angles comprise a distribution of directions on the unit sphere which we plot here using Lambert's equal area projection. The radius is the angle from 0° at the centre to 90° at the edge, and the azimuth is the direction of tilt. The cross marks the true tilt direction. The proportion of tilt pairs that cluster around the true tilt direction (∼30/823) is consistent with the proportion of particles kept after 3D classification that were used in the final reconstruction (∼8%). (**C**) Histogram of the local resolution of the map in real space calculated using ResMap (*36*).

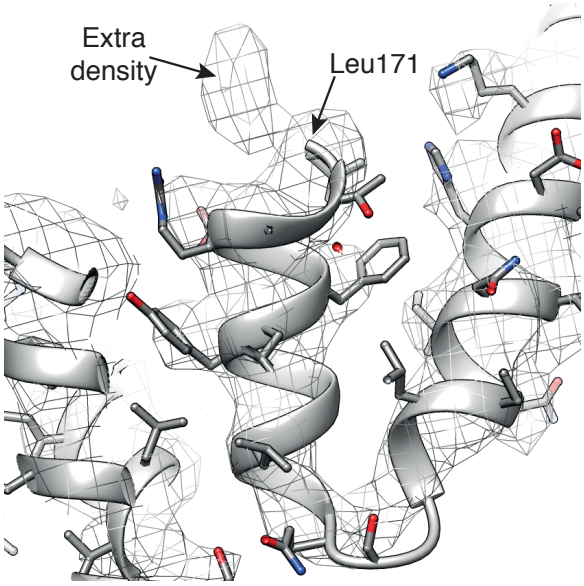

Fig. S8: **Map and model showing extra density at the C-terminus.** The refined apoferritin co-ordinates were fit to the cryo-EM density map. Extra density is present at the C-terminus. Apoferritin has an additional three amino acids (K172, H173, D174) at the C-terminus which were not modeled in this crystal structure (PDB 2W0O, (*25*)) but are present in the sequence.

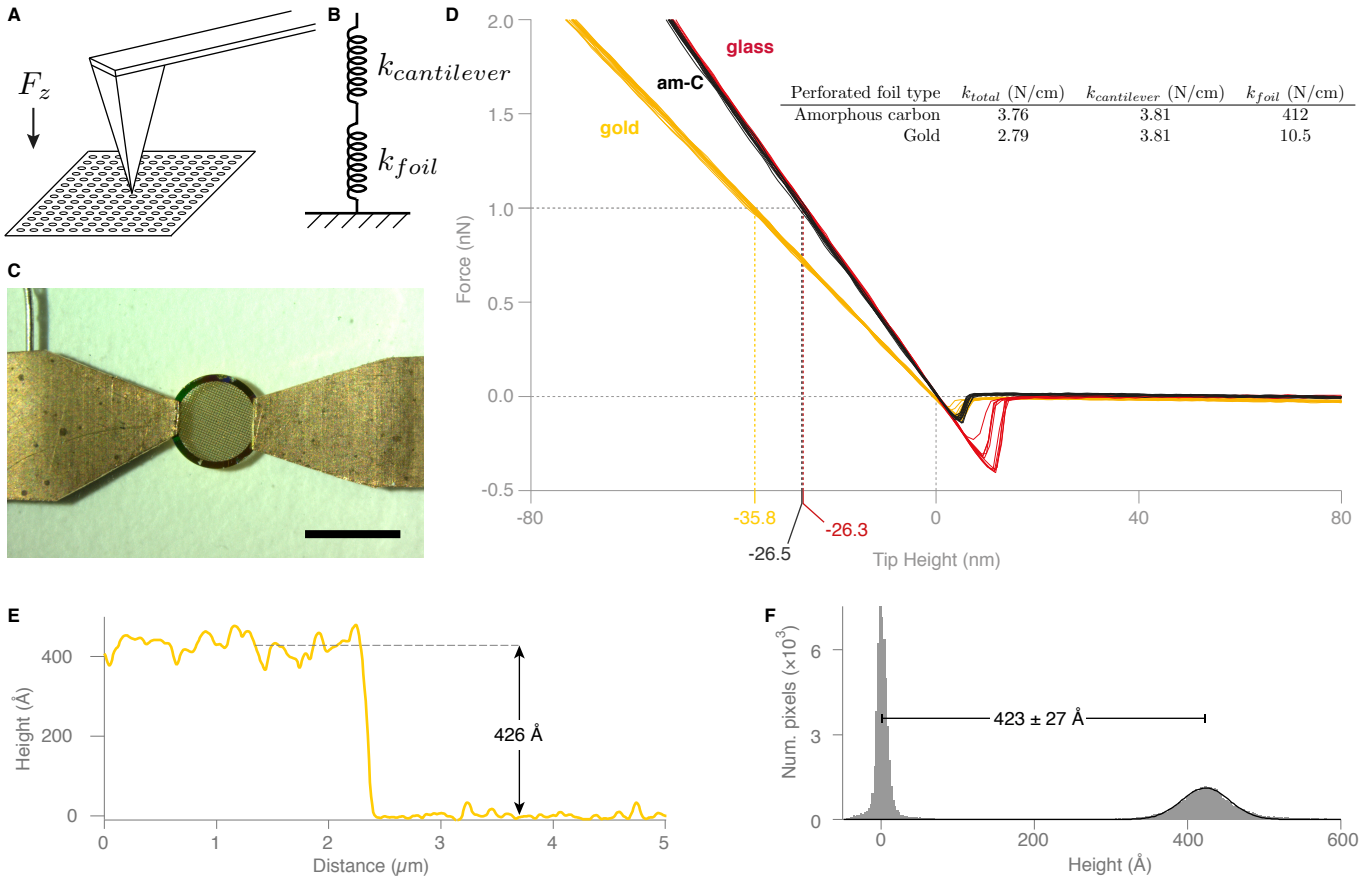

Fig. S9: **Support foil flexural rigidity** To measure the flexural rigidity of perforated foils suspended within a square of the grid support mesh, an AFM (Asylum MFP3D) was used to apply pressure to the centre of the suspended foil in a grid square and measure the force response (**A**). The force vs. height of the system is modelled as two springs in series (**B**), and was measured using a custom apparatus that firmly clips the grids in place on the microscope stage (**C**). The force constant of the cantilever was measured using the the thermal resonance spectra of the tip/cantilever and the deflection vs. position for the tip when pressed on a hard surface (glass, red curve in **D**). Using this one can then measure the difference in the force response of the amorphous carbon vs. the gold foils. Each force curve was repeated 10 times on each surface, fit using linear regression, and the average of the slopes taken as the spring constant k. The results are tabulated in the inset in **D**. At room temperature, the amorphous carbon film has a ∼40-fold higher flexural rigidity than the gold foil. The average thickness of the gold foil used for this analysis was also measured as described above, (**E-F**) and was 422.5 ± 0.3 Å.

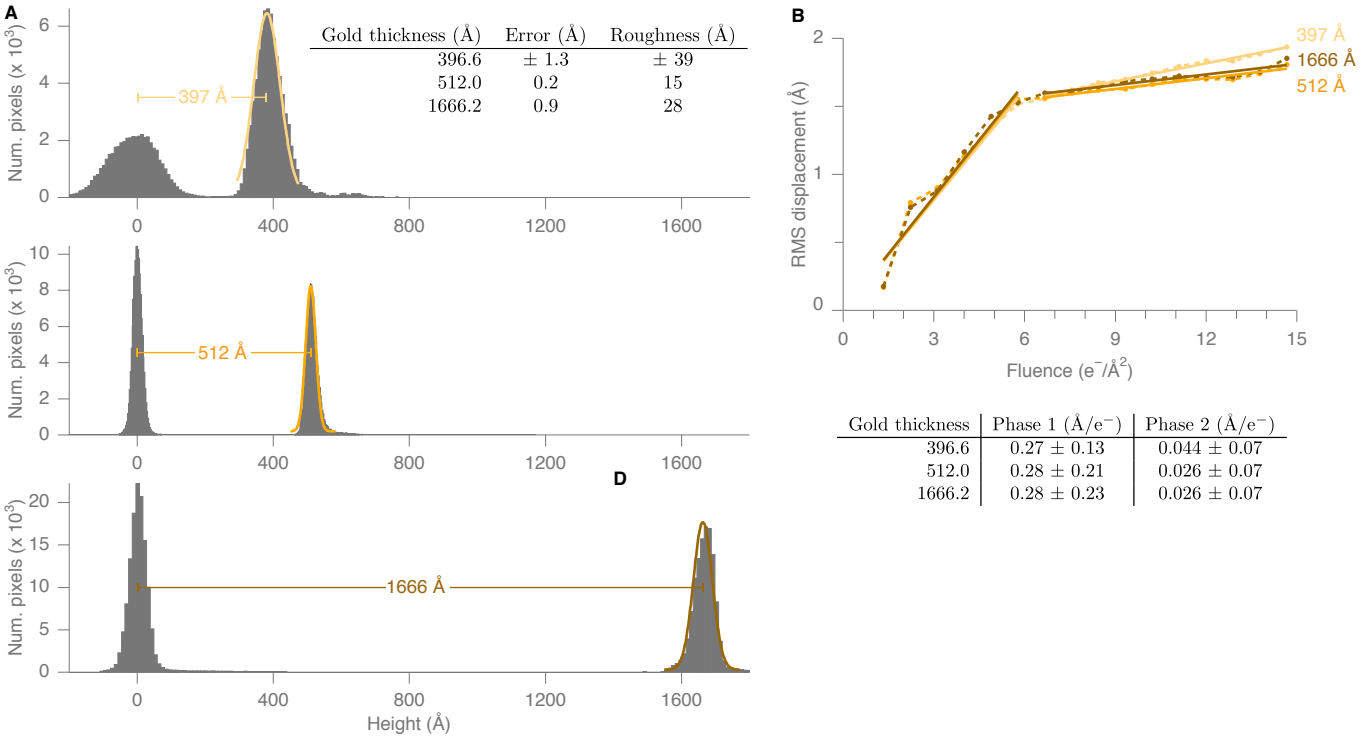

Gold thickness (Å)	Error (Å)	Roughness (Å)
396.6	± 1.3	± 39
512.0	0.2	15
1666.2	0.9	28

Gold thickness	Phase 1 (Å/e⁻)	Phase 2 (Å/e⁻)
396.6	0.27 ± 0.13	0.044 ± 0.07
512.0	0.28 ± 0.21	0.026 ± 0.07
1666.2	0.28 ± 0.23	0.026 ± 0.07

Fig. S10: **Speed plots for gold supports of varying thickness.** Constant-force mode atomic force microscopy was used to measure the thickness of three different gold layers used to make perforated gold foils. (**A**) Histograms of height values, with Gaussian fits to determine the average thickness of the gold layers. The standard deviation of the gold height is taken as the approximate roughness of the foil, and the composite error of locating the positions of the peaks was taken as the error in the average thickness. The absolute error in the calibration of the z channel of the microscope is $\leq 1\%$. 80S ribosome datasets were collected on supports of each thickness, the particle motions were tracked for each grid and speed plots were generated as described in the methods (**B**) and the speeds are tabulated. The performance of the grids is consistent for the several different thickness foils, with an increase in the second phase speed for the thinnest support.

Supplementary movie

Reduced motion of gold substrates during high-energy electron irradiation Movies of am-C and gold supports (without ice) under typical cryo-EM illumination conditions (300 keV, 16 $e^-/Å^2/s$ and 80K with a nominal defocus of -2 μm) where the support was tilted to 30°. The movies were collected on a Falcon II direct electron detector at 18 frames per second for 4 seconds. Upper panels show the entire 1.2 μm diameter holes during irradiation. Lower panels show a magnified view of the edge of each hole which is parallel to the tilt axis. The displacements of the edges of holes in the foil were tracked relative to their initial positions before electron irradiation, and used to measure the vertical displacement of the support (Fig. 2). Scale bars (white) correspond to 1200 Å (upper panels) and 120 Å (lower panels).

Supplementary table

Table 1: **Data, refinement and model statistics**

Data collection	
Number of particles	483
Number of asymmetric units	11 592
Pixel size	1.346 Å
Defocus range	1.6−4.7 μm
Mean defocus	2.87 μm
Energy	300 keV
Electron flux	16.0 $e^-/Å^2/s$
Electron fluence	15.5 $e^-/Å^2$
Specimen temperature	≃80K
Particle box size	$(132 \text{ px})^3$
Model composition	
Number of asymmetric units (Symmetry)	24 (432)
Non-hydrogen atoms	32 736
Protein residues	4080
Refinement	
Resolution range	177−4.5 Å
R-factor	0.289
Fourier Shell Correlation (map vs. refined model at 0.5)	4.71
RMS deviations	
Bonds	0.019 Å
Angles	2.53°
Validation	
Molprobity score	2.24 (100th percentile)
Clashscore, all atoms	7.78 (97th percentile)
Good rotamers	94.1%
Ramachandran plot	
Favored	96.5%
Outliers	0.6%

References

1. A. Amunts, *et al.*, Structure of the yeast mitochondrial large ribosomal subunit. *Science* **343**, 1485–1489 (2014).

2. M. Liao, E. Cao, D. Julius, Y. Cheng, Structure of the TRPV1 ion channel determined by electron cryo-microscopy. *Nature* **504**, 107–112 (2014).

3. M. Allegretti, D. J. Mills, G. McMullan, W. Kuhlbrandt, J. Vonck, Atomic model of the F420-reducing [NiFe] hydrogenase by electron cryo-microscopy using a direct electron detector. *eLife* **3**, e01963–e01963 (2014).

4. R. Henderson, The potential and limitations of neutrons, electrons and X-rays for atomic resolution microscopy of unstained biological molecules.. *Q. Rev. Biophys.* **28**, 171–193 (1995).

5. P. B. Rosenthal, R. Henderson, Optimal determination of particle orientation, absolute hand, and contrast loss in single-particle electron cryomicroscopy. *J. Mol. Biol,* **333**, 721 – 745 (2003).

6. R. Henderson, G. McMullan, Problems in obtaining perfect images by single-particle electron cryomicroscopy of biological structures in amorphous ice. *Microscopy* **62**, 43–50 (2013).

7. A. Faruqi, *et al.*, Direct single electron detection with a CMOS detector for electron microscopy. *Nucl. Instrum. Methods* **546**, 170–175 (2005).

8. R. Henderson, R. M. Glaeser, Quantitative analysis of image contrast in electron micrographs of beam-sensitive crystals. *Ultramicroscopy* **16**, 139 – 150 (1985).

9. E. R. Wright, C. V. Iancu, W. F. Tivol, G. J. Jensen, Observations on the behavior of vitreous ice at ≃82 and ≃12K. *J. Struct. Biol.* **153**, 241–252 (2006).

10. R. M. Glaeser, G. McMullan, A. R. Faruqi, R. Henderson, Images of paraffin monolayer crystals with perfect contrast: minimization of beam-induced specimen motion. *Ultramicroscopy* **111**, 90–100 (2011).

11. A. F. Brilot, *et al.*, Beam-induced motion of vitrified specimen on holey carbon film. *J. Struct. Biol.* **177**, 630–637 (2012).

12. G. McMullan, S. Chen, R. Henderson, A. R. Faruqi, Detective quantum efficiency of electron area detectors in electron microscopy. *Ultramicroscopy* **109**, 1126–1143 (2009).

13. G. McMullan, A. R. Faruqi, D. Clare, R. Henderson, Comparison of optimal performance at 300 keV of three direct electron detectors for use in low dose electron microscopy. *Ultramicroscopy* **147**, 156–163 (2014).

14. M. G. Campbell, *et al.*, Movies of ice-embedded particles enhance resolution in electron cryo-microscopy. *Structure* **20**, 1823–1828 (2012).

15. X.-C. Bai, I. S. Fernandez, G. McMullan, S. H. Scheres, Ribosome structures to near-atomic resolution from thirty thousand cryo-EM particles. *eLife* **2**, e00461 (2013).

16. X. Li, *et al.*, Electron counting and beam-induced motion correction enable near-atomic-resolution single-particle cryo-EM. *Nat. Methods* **10**, 584–590 (2013).

17. C. J. Russo, L. A. Passmore, Controlling protein adsorption on graphene for cryo-EM using low-energy hydrogen plasmas. *Nat. Methods* **11**, 649–652 (2014).

18. D. Rhinow, W. Kühlbrandt, Electron cryo-microscopy of biological specimens on conductive titanium-silicon metal glass films. *Ultramicroscopy* **108**, 698–705 (2008).

19. C. Yoshioka, B. Carragher, C. S. Potter, Cryomesh: a new substrate for cryo-electron microscopy. *Microsc. Microanal.* **16**, 43–53 (2010).

20. C. J. Russo, L. A. Passmore, Robust evaluation of 3D electron cryomicroscopy data using tilt-pairs. *J. Struct. Biol.* **187**, 112–118 (2014).

21. S. H. Banyard, D. K. Stammers, P. M. Harrison, Electron density map of apoferritin at 2.8 Å resolution. *Nature* **271**, 282–284 (1978).

22. R. R. Crichton, J.-P. Declercq, X-ray structures of ferritins and related proteins. *Biochim. Biophys. Acta* **1800**, 706–718 (2010).

23. W. H. Massover, Ultrastructure of ferritin and apoferritin: a review. *Micron* **24**, 389–437 (1993).

24. S. H. W. Scheres, RELION: implementation of a bayesian approach to cryo-EM structure determination. *J. Struct. Biol.* **180**, 519–530 (2012).

25. N. de Val, J.-P. Declercq, C. K. Lim, R. R. Crichton, Structural analysis of haemin demetallation by L-chain apoferritins. *J. Inorg. Biochem.* **112**, 77–84 (2012).

26. W. Baumeister, M. Hahn, J. Seredynski, L. M. Herbertz, Radiation damage of proteins in the solid state: changes of amino acid composition in catalase. *Ultramicroscopy* **1**, 377–382 (1976).

27. H. Stark, F. Zemlin, C. Boettcher, Electron radiation damage to protein crystals of bacteriorhodopsin at different temperatures. *Ultramicroscopy* **63**, 75–79 (1996).

28. J. L. Hutter, J. Bechhoefer, Calibration of atomic-force microscope tips. *Rev. Sci. Instrum.* **64**, 1868 (1993).

29. C. A. Schneider, W. S. Rasband, K. W. Eliceiri, NIH Image to ImageJ: 25 years of image analysis. *Nat. Methods* **9**, 671–675 (2012).

30. J. A. Mindell, N. Grigorieff, Accurate determination of local defocus and specimen tilt in electron microscopy. *J. Struct. Biol.* **142**, 334–347 (2003).

31. R. Henderson, *et al.*, Tilt-pair analysis of images from a range of different specimens in single-particle electron cryomicroscopy. *J. Mol. Biol.* **413**, 1028–1046 (2011).

32. S. H. Scheres, Beam-induced motion correction for sub-megadalton cryo-EM particles. *eLife* **3**, e03665 (2014).

33. T. Granier, B. Gallois, A. Dautant, B. Langlois d'Estaintot, G. Précigoux, Comparison of the structures of the cubic and tetragonal forms of horse-spleen apoferritin. *Acta Crystallogr. D* **53**, 580–587 (1997).

34. P. Lu, *et al.*, Three-dimensional structure of human γ-secretase. *Nature* **512**, 166–170 (2014).

35. R. Marabini, *et al.*, Xmipp: An image processing package for electron microscopy. *J. Struct. Biol.* **116**, 237 – 240 (1996).

36. A. Kucukelbir, F. J. Sigworth, H. D. Tagare, Quantifying the local resolution of cryo-EM density maps. *Nat. Methods* **11**, 63–65 (2014).

37. A. Vagin, A. Teplyakov, MOLREP: an automated program for molecular replacement. *J. Appl. Crystallogr.* **30**, 1022–1025 (1997).

38. G. N. Murshudov, *et al.*, REFMAC5 for the refinement of macromolecular crystal structures. *Acta Crystallogr. D* **67**, 355–367 (2011).

39. E. F. Pettersen, *et al.*, UCSF chimera–a visualization system for exploratory research and analysis. *J. Comput. Chem.* **25**, 1605–1612 (2004).

40. L. D. Landau, E. M. Lifshitz, *Theory of Elasticity* vol. 3 of *Course of Theoretical Physics* (Butterworth Heinemann, 1986) third edn.